Supplementary Information for

Cooperative coupling of anisotropic phonon modes intensifies visible thermochromism in layered α-MoO_3

Youngkwang Kim[1),#], June Ho Lee[1),#], Young Hwa Jung[2)], Donghwa Lee[1),*] and Junwoo Son[1),*]

1) Department of Materials Science and Engineering (MSE), Pohang University of Science and Technology (POSTECH), Pohang 37673, Republic of Korea

2) Pohang Accelerator Laboratory, Pohang 37673, Republic of Korea

[#] These authors contributed equally to this work.

[*]jwson@postech.ac.kr, donghwa96@postech.ac.kr

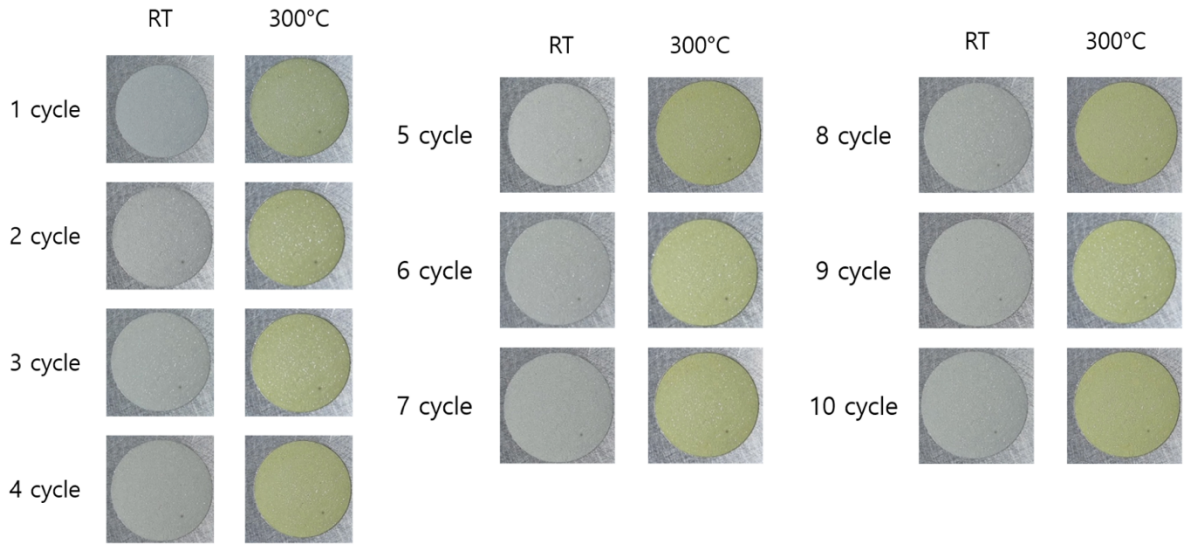

Figure S1 | photographs of color changes of α-MoO_3 during ten times of heating-cooling sweep. the α-MoO_3 samples changed from white into (greenish) yellow upon heating and then restored white upon cooling; This change is highly reproducible under an ambient atmosphere up to ten times of heating-cooling sweep.

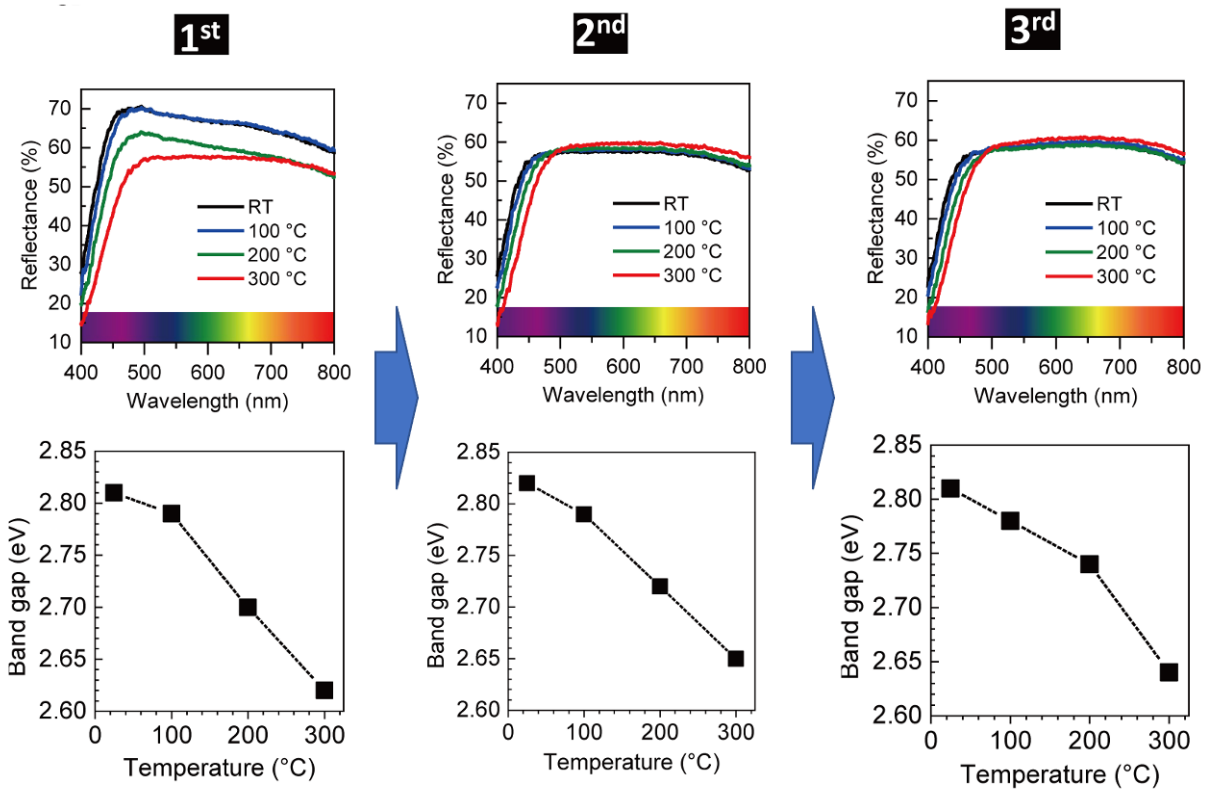

Figure S2 | temperature-dependent diffuse reflectance spectra and estimated band gap from the Tauc's relationship as a function of temperature at the 1st, 2nd, 3rd heating-cooling sweeps.

First of all, the shift of the absorption edge and corresponding band gap was fully reversible in the 2nd and 3rd consecutive heating/cooling cycle.

Secondly, slight irreversible change of thermochromism was observed in terms of quantitative analysis of color changes ($L^*a^*b^*$ parameters) of α-MoO_3 during initial (1st) and subsequent (2nd) heating and cooling sweep in Fig. 1. Namely, $L^*a^*b^*$ parameters at room temperature was increased to 3.23 after 1st heating and cooling sweep.

Indeed, we also characterized this slight non-reversibility during 1st heating and cooling sweep by the diffuse reflectance spectrum. Higher reflectance was observed in the 1st sweep than in the 2nd sweep. The initial reflectance was not recovered after 1st heating and cooling sweep.

We think that the irreversible component of reflectance spectra appears to be related to the residual impurities after the synthesis of α-MoO_3. For example, α-MoO_3 is likely to adsorb water molecules and/or volatile by-product related with nitrates and ammonium decomposition, which are detached at the temperature between 30 to 130 °C and/or between 130 to 250 °C, respectively, during heating

process (*AIP Conf. Proc.* 2265, 030716 (2020)). Considering the purity of our α-MoO_3 powder (99.98 %), significant amounts of impurities are incorporated in an initial state, which also influence crystal structure and optical properties; these impurities are irreversibly removed as the temperature is increased. Once the impurities are fully removed after the 1st heating and cooling sweep, the fully reversible optical thermochromic behavior was observed; these unwanted impurity in as-received α-MoO_3 is likely to contribute the irreversible optical property.

	R	G	B	L*	a*	b*	ΔEab
25 °C-1	190	195	189	78.55	-0.74	-3.18	0.00
100 °C-1	182	188	170	75.58	-3.55	3.26	7.63
200 °C-1	168	175	151	70.54	-5.24	6.81	13.57
300 °C-1	178	180	118	71.96	-9.50	27.77	32.83
25 °C-2	186	188	179	76.13	-0.39	-1.06	3.24
100 °C-2	191	194	178	78.06	-2.04	2.37	5.72
200 °C-2	189	194	157	77.38	-6.57	13.31	17.54
300 °C-2	190	195	130	77.17	-10.93	28.19	33.01

Table S1 | Table of *L*a*b** parameters from image analysis during 1st and 2nd heating procedure. For quantitative analysis of color changes, the *L*a*b** parameters have been extracted from all photographs. Theses parameters were first converted to the linear RGB parameters and then to the XYZ parameter in CIE 1931 XYZ color space, accompanied by conversion to L*a*b* parameters.

	Atom	Wyckoff	*x*	*y*	*z*	occ	U_{iso}
25 °C-1	Mo1	4*c*	0.0717(4)	0.1023(1)	0.25	0.99(3)	0.035(1)
	O1	4*c*	0.4782(23)	0.4373(3)	0.25	1.07(3)	0.036(3)
	O2	4*c*	0.5703(24)	0.0904(3)	0.25	1.12(3)	0.048(3)
	O3	4*c*	0.0465(21)	0.2089(3)	0.25	0.96(3)	0.020(2)
300 °C	Mo1	4*c*	0.0726(4)	0.1010(1)	0.25	0.98(1)	0.027(1)
	O1	4*c*	0.5004(21)	0.4317(3)	0.25	1.07(2)	0.007(2)
	O2	4*c*	0.5990(30)	0.0877(4)	0.25	1.12(2)	0.092(4)
	O3	4*c*	0.0523(23)	0.2099(3)	0.25	0.94(2)	0.019(2)
25 °C-2 (after 300 °C)	Mo1	4*c*	0.0720(4)	0.1019(1)	0.25	1.00(1)	0.028(1)
	O1	4*c*	0.4941(25)	0.4363(3)	0.25	1.11(2)	0.023(3)
	O2	4*c*	0.5846(27)	0.0866(4)	0.25	1.08(2)	0.045(3)
	O3	4*c*	0.0616(24)	0.2100(3)	0.25	0.93(2)	0.016(2)

Table S2 | Refined atomic parameters of α-MoO_3 at different temperature using synchrotron powder XRD data and Rietveld refinements (PAL II-BL9B, λ = 1.5216 Å).

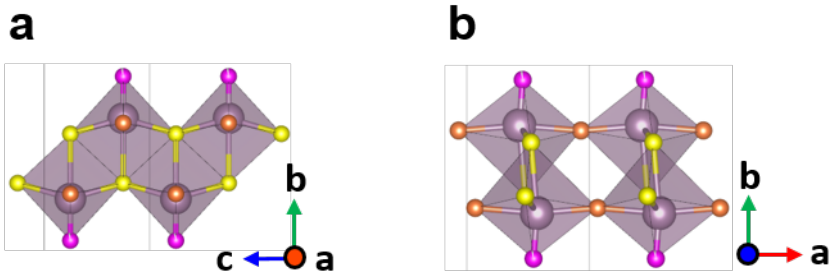

Figure S3 | Schematic image of **a,** edge sharing and **b,** corner sharing in intra-layer [MoO_6] octahedron of α-MoO_3. The yellow colored oxygen ions ($O_1^{eq.1}$, $O_1^{eq.2}$, $O_1^{ap.}$) are located at the edge sharing, the orange colored oxygen ions ($O_2^{eq.1}$, $O_2^{eq.2}$) are located at the corner sharing. These unique layered-structure could induce anisotropic thermal expansion and visible thermochromism.

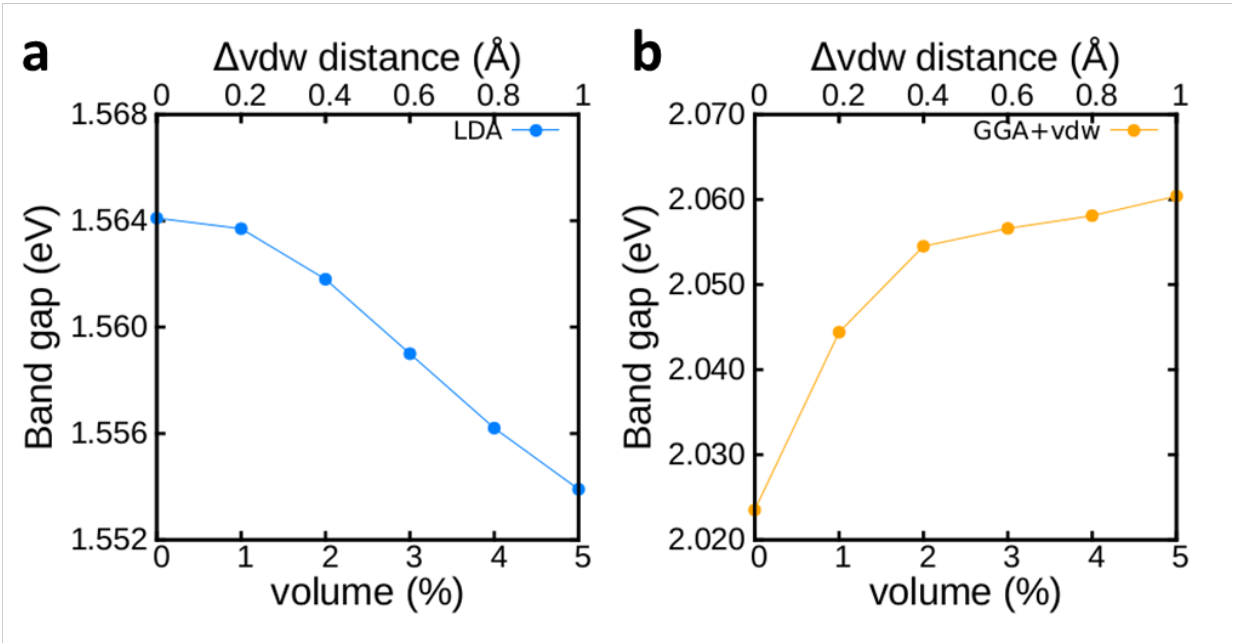

Figure S4 | Band gap vs volume expansion of α-MoO_3 calculated by **a,** LDA and **b,** GGA+U method. Atomic positions are fully relaxed at each expanded volume. For the LDA method, the bandgap decreases only by 0.01 eV for 1 Å increase in the VdW layer distance that is equivalent to the 5 % volume expansion. With the GGA+U method, the bandgap increases only by 0.04 eV for 1 Å increase in the VdW layer distance. These small change in band gap indicate that the change in VdW distance is not the main origin of the bandgap reduction at high temperature.

.

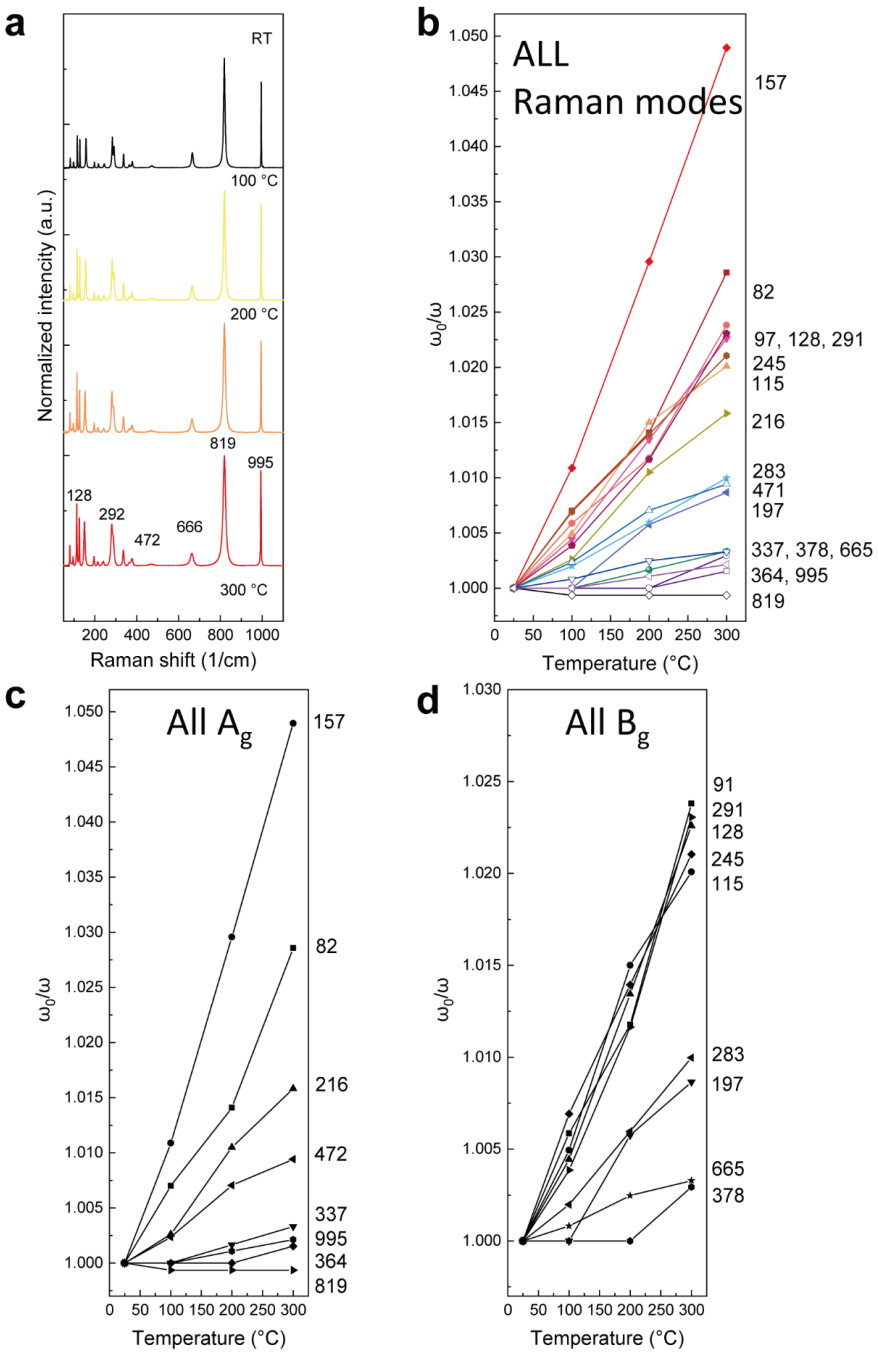

Figure S5 | a, temperature-dependent Raman spectroscopy of α-MoO_3. Relative Raman frequency shift of all Raman modes (**b**), all A_g modes (**c**) and all B_g modes (**d**) in α-MoO_3. We selected specific Raman modes that is responsible for the visible thermochromism from all Raman modes in α-MoO_3.

D_{2h}	E	$C_2(z)$	$C_2(y)$	$C_2(x)$	i	σ (xy)	σ (xz)	σ (yz)		
A_g	1	1	1	1	1	1	1	1	x^2, y^2, z^2	Raman
B_{1g}	1	1	-1	-1	1	1	-1	-1	xy, J_z	Raman
B_{2g}	1	-1	1	-1	1	-1	1	-1	xz, J_y	Raman
B_{3g}	1	-1	-1	1	1	-1	-1	1	yz, J_x	Raman
A_u	1	1	1	1	1	-1	-1	-1		
B_{1u}	1	1	-1	-1	1	-1	1	1	z	IR
B_{2u}	1	-1	1	-1	1	1	-1	1	y	IR
B_{3u}	1	-1	-1	1	1	1	1	-1	x	IR

Table S3 | Character table for point group D_{2h} (mmm)**.** The sign of each character indicate that symmetry operations are preserved (plus) and broken (minus). A_g, B_{1g}, B_{2g} and B_{3g} modes are Raman active, and B_{1u}, B_{2u} and B_{3u} modes are IR active. Among four Raman active modes (A_g, B_{1g}, B_{2g} and B_{3g}), A_g mode fully preserve 8 symmetry operations, whereas B_{ng} (n : 1, 2, 3) modes break the 2 of 3 rotation and 2 of 3 mirror symmetry operation.

Mode	Ref [1] (cm^{-1})	Ref [2] (cm^{-1})	Exp. (cm^{-1})	Cal. (cm^{-1})	Induced phase
A_g	83	84	82	77.85	*Pbnm*
	158	162	157	159.28	
	217	230	216	222.82	
	337	327	337	319.01	
	365	365	364	341.72	
	473	473	472	453.30	
	819	822	819	723.53	
	995	998	995	1009.20	

Mode	Ref [1] (cm^{-1})	Ref [2] (cm^{-1})	Exp. (cm^{-1})	Cal. (cm^{-1})	Induced phase
B_{1g}	99	102	97	96.32	$P2_1/m$
	379	386	378	355.78	
B_{2g}	116	118	115	105.88	$P2_1/c$
	198	200	197	198.51	
	283	285	283	259.76	
B_{3g}	129	138	128	124.96	$P2_1/c$
	246	257	245	237.47	
	291	290	291	283.11	
	666	668	665	650.86	

Table S4 | Experimental and calculated Raman modes. A_g modes preserves their original structure (*Pbnm*), while the other modes cause a phase transition ($P2_1/m$ for B_{1g} modes, $P2_1/c$ for B_{2g} and B_{3g} modes). Experimental and calculated results are well matched with prior results[1,2]

[1] L. Seguin, M. Figlarz, R. Cavagnat, J. C. Lassegues. Infrared and Raman spectra of MoO_3 molybdenum trioxides and $MoO_3 \cdot xH_2O$ molybdenum trioxide hydrates, *Spectrochim. Acta A*, **51**, 1323, (1995)

[2] M.A. PY, K. Maschke, Intra- and Interlayer Contributions to the lattice vibrations in MoO_3, *Physica*, 105B, 370-374, (1981)

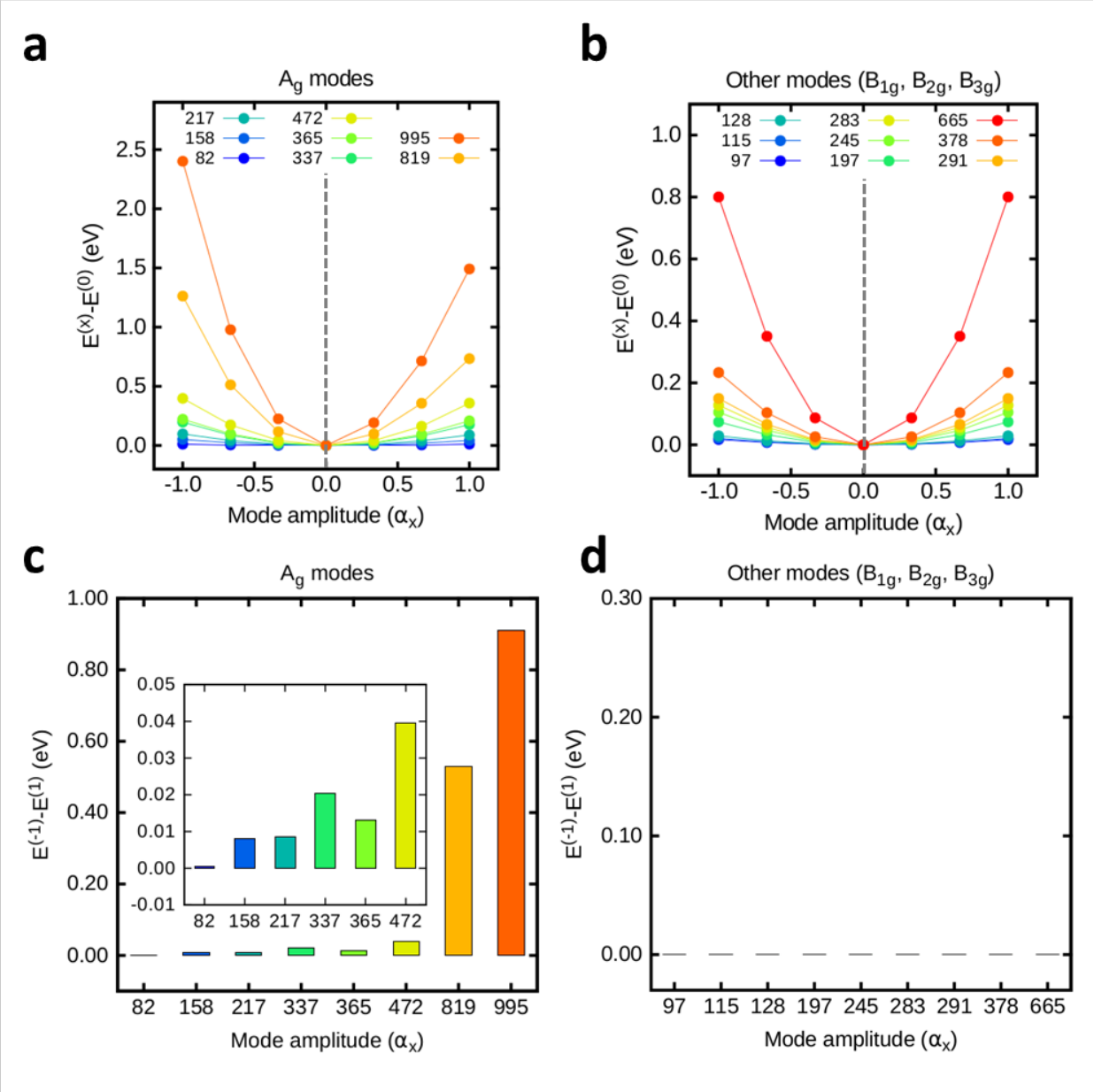

Figure S6 | Relative Kohn-Sham (KS) energies as a function of Raman mode amplitude. Relative KS energy as a function of Raman mode amplitude α_x for **a,** A_g and **b,** other (B_{1g}, B_{2g}, B_{3g}) modes. KS energy difference between the structures with α_x = -1 and 1 amplitude for **c,** A_g and **d,** other (B_{1g}, B_{2g}, B_{3g}) modes. As shown **Figure S4 c-d** A_g modes exhibits asymmetric potential while other modes (B_{1g}, B_{2g}, B_{3g}) have symmetric potential as the displacement vector is changed.

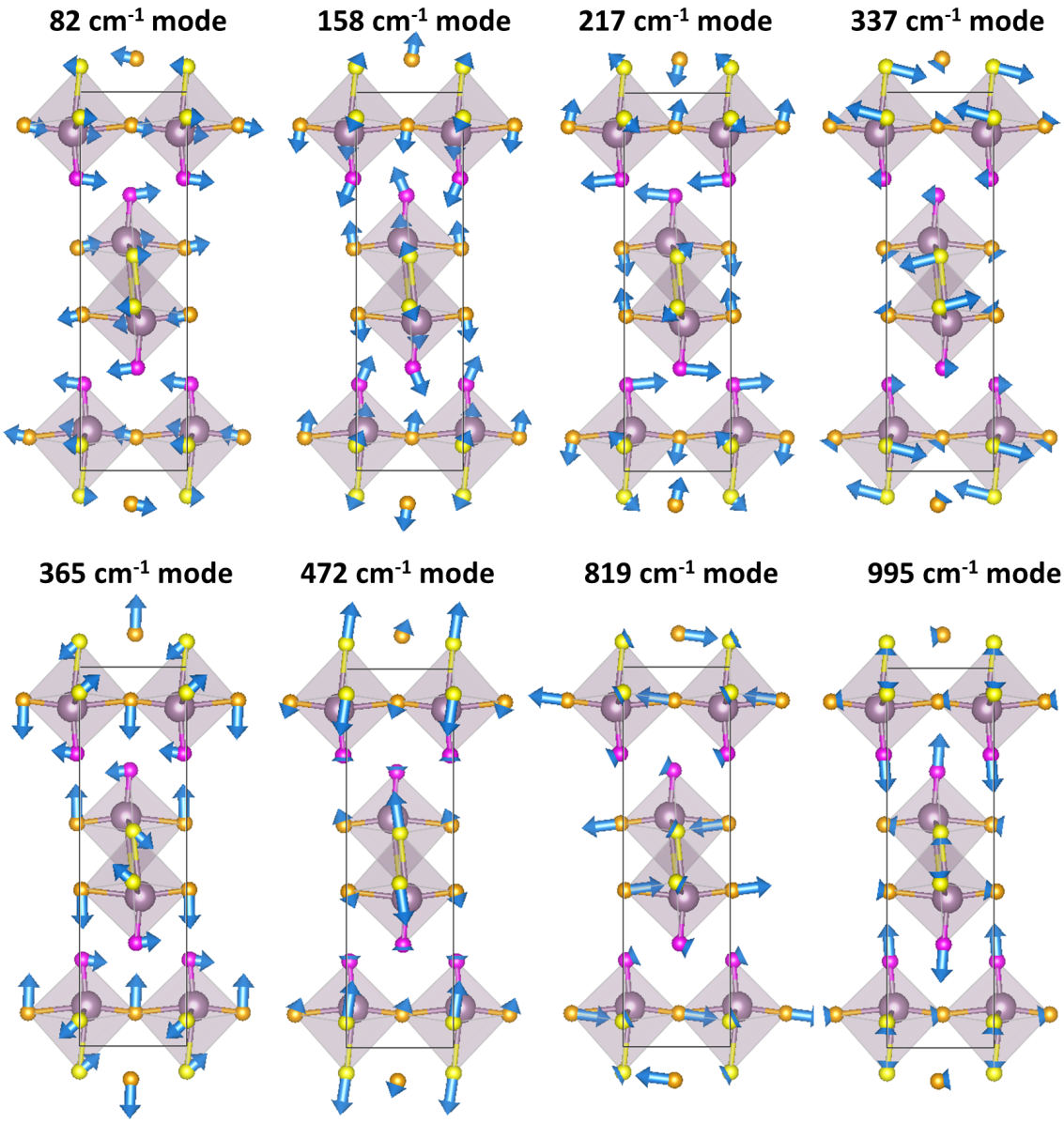

Figure S7 | Displacement vectors of each A_g modes. Displacement vector (blue arrow) of each A_g (82, 158, 217, 337, 365, 472, 819, 995) modes.

		Structural variation.	
		Exp. (%)	Cal. (471 + 995 mode) (%)
Apical	$Mo\text{-}O_1^{ap}$	3.510	4.630
	$Mo\text{-}O_3^{ap}$	2.003	2.680
Equatorial	$Mo\text{-}O_1^{eq.1}$	-1.130	-2.026
	$Mo\text{-}O_1^{eq.2}$	-1.130	-2.026
	$Mo\text{-}O_2^{eq.1}$	2.793	1.028
	$Mo\text{-}O_2^{eq.2}$	-2.676	-1.602

Table S5 | Variation of experimental and calculated bond length in MoO_6 octahedron. The calculated structural variation with the coupled contribution of 472 (with 1.2 amplitude) and 995 (with 0.4 amplitude) mode was well-matched with the experimental structural variation.

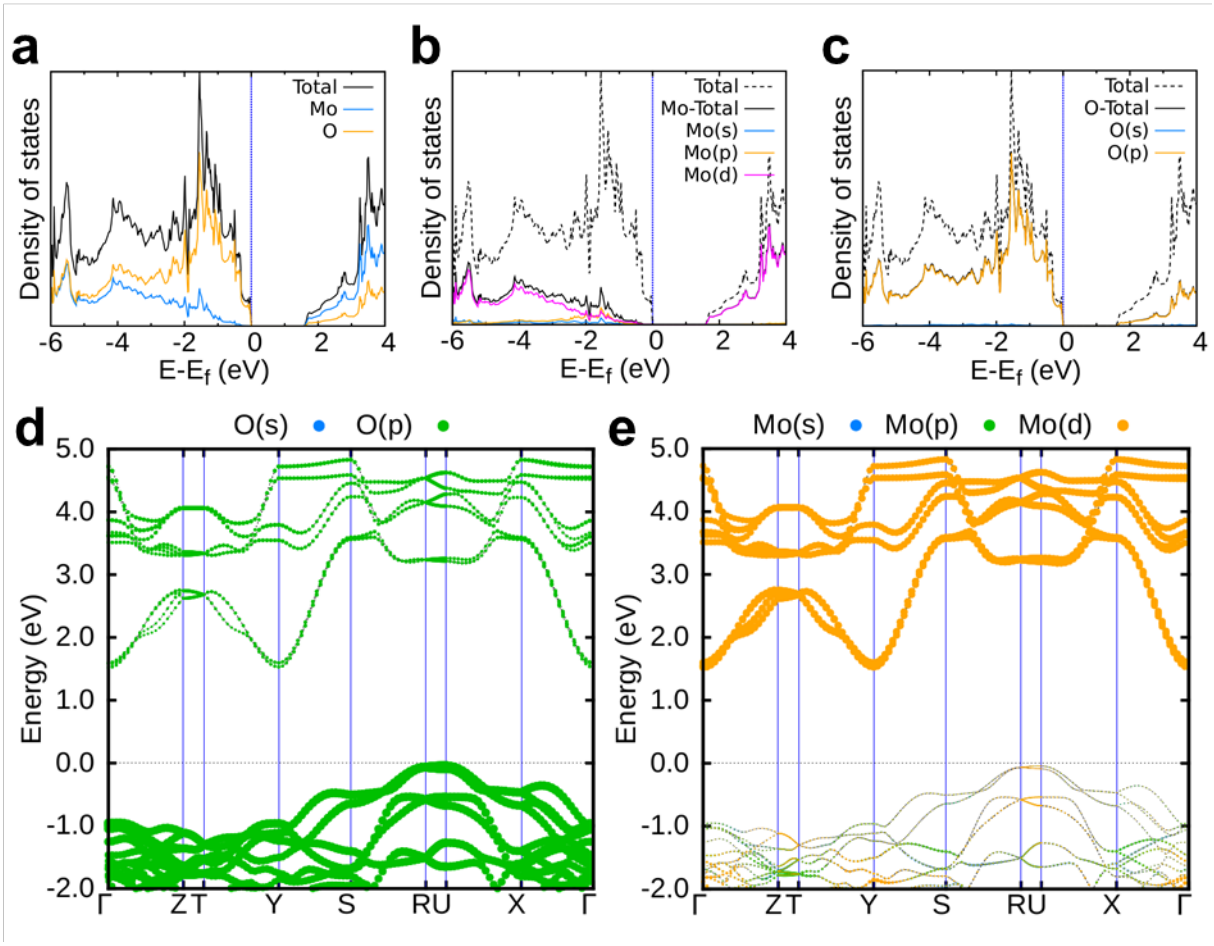

Figure S8 | Electronic structure of α-MoO_3. **a,** Densify of states **b,** Mo orbital decomposed and **c,** O orbital decomposed density of states of MoO_3 structure. **d,** O orbital and **e,** Mo orbital projected-band structure of MoO_3 structure. Valence band maximum / Conduction band minimum is located at U points / Γ point. Valence / Conduction band near the Fermi level is composed of O(p) / hybridized Mo(d)-O(p) orbital.

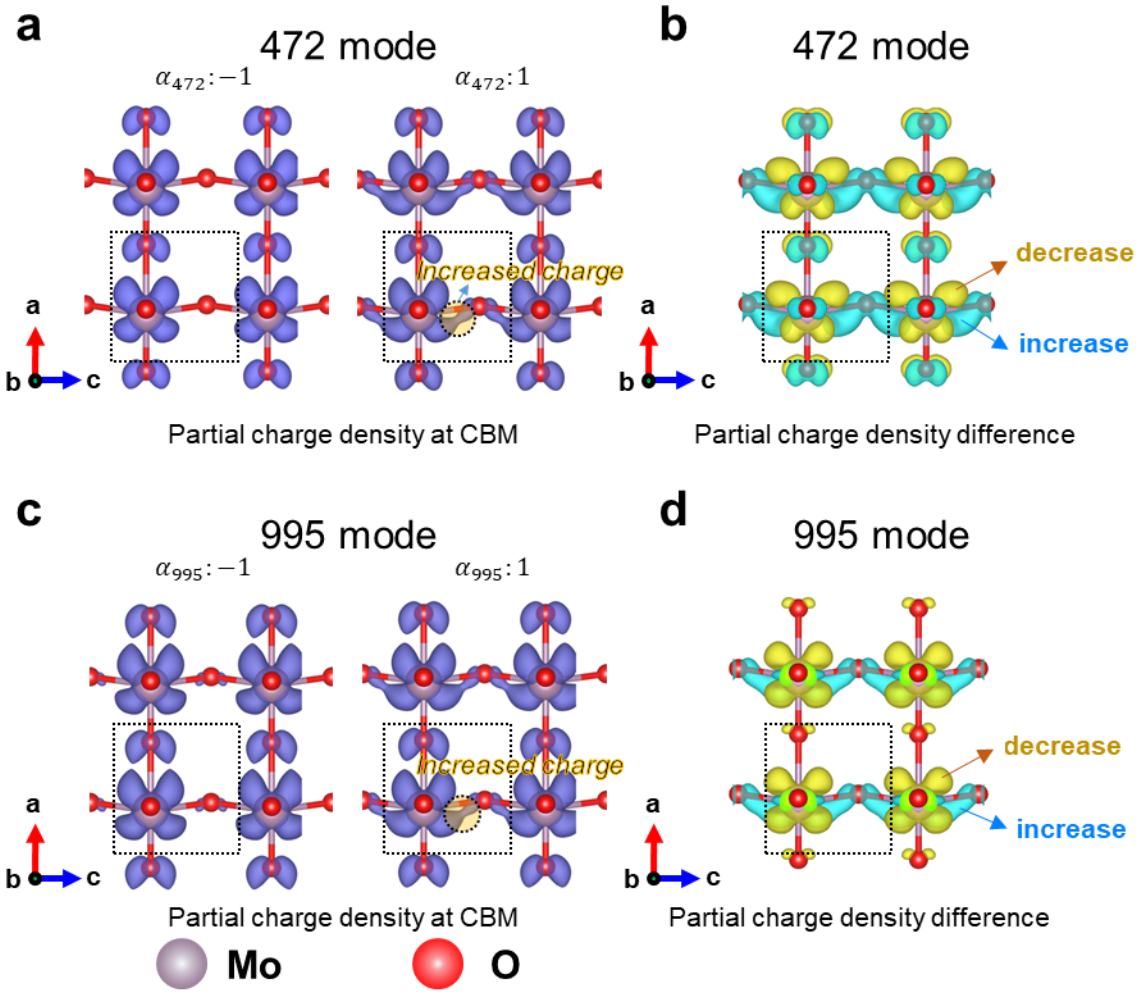

Figure S9 | Partial charge density at CBM of 472 and 995 modes. Partial charge density (blue) at CBM with different mode amplitude (α_x : -1 and 1) for **a,** 472 and **c,** 995 modes. Orange dot circle indicates increased charge density between Mo and O atom. The spatial charge density difference in CBM between the structures with different mode amplitude (α_x : -1 and 1) for **b,** 472 and **d,** 995 modes. Cyan/yellow indicate increased / decreased partial charge density. The orbital overlap of the Mo 4*d* – O 2*p* hybridized state along the c-axis is enhanced with increasing α_{472} and α_{995}.

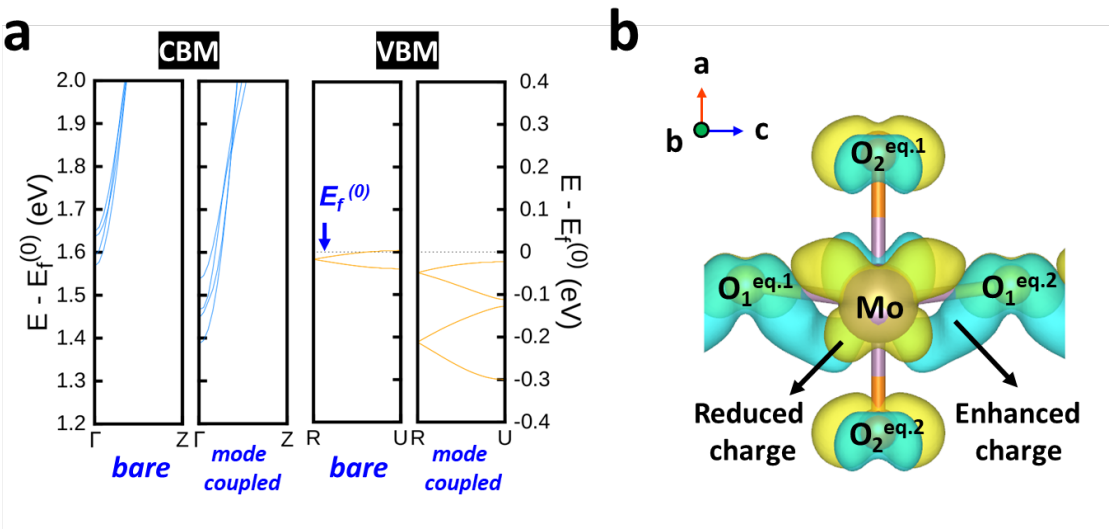

Figure S10 | Partial charge density at CBM of 472 and 995 modes**. a,** Comparison of CBM (left), VBM(right) for the bare- and mode coupled-structure. **b,** The spatial charge density difference in CBM between the bare- and mode coupled- structure. For the mode coupled (472 and 995 modes) structure, the effect of mode on the band gap reduction is maintained.

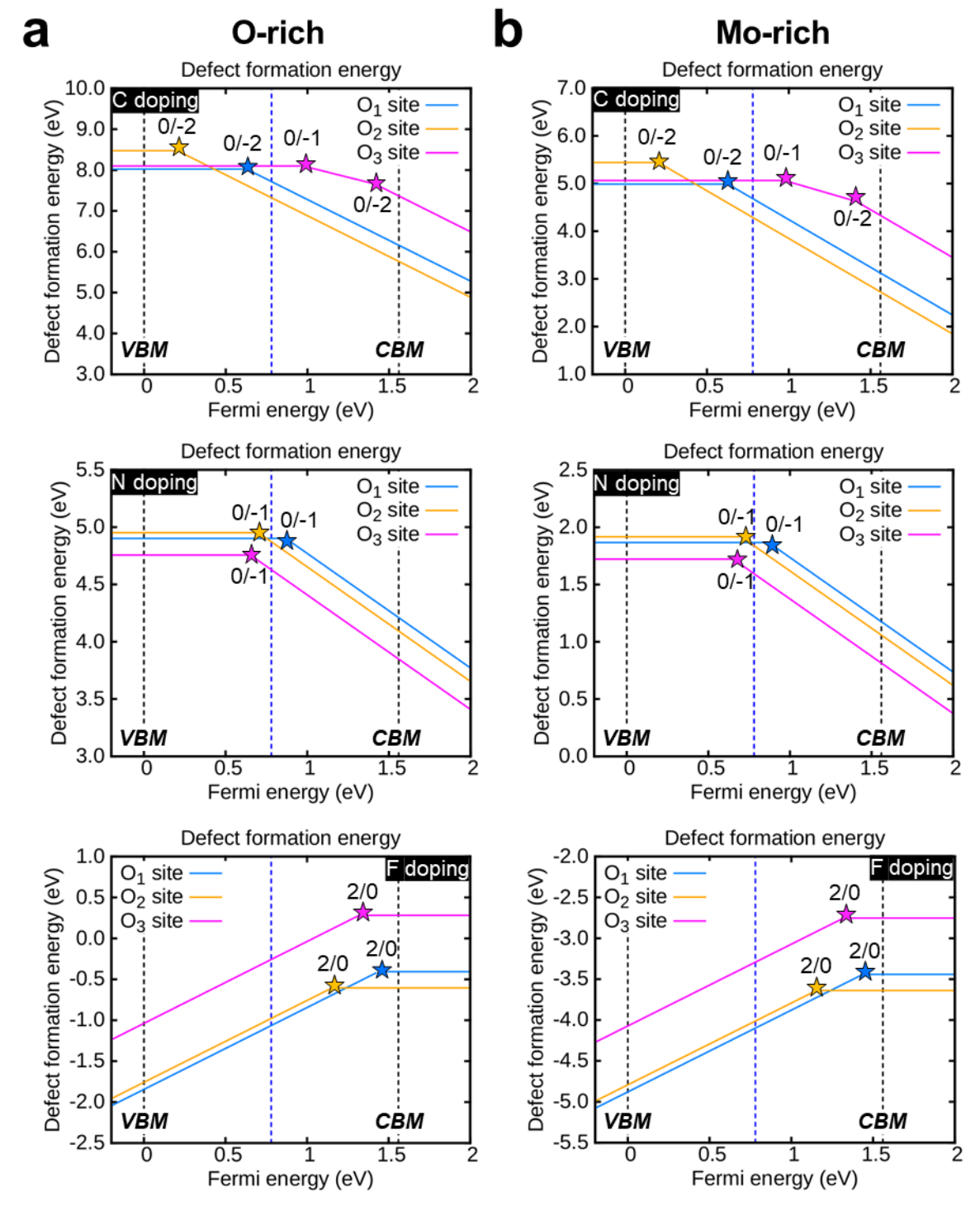

Figure S11 | Defect formation energies of substitutional anion defects. Defect formation energies of substitutional C (top), N (middle), and F (bottom) defects on O_1 (blue), O_2 (orange), and O_3 (magenta) sites under a. O-rich and b. Mo-rich conditions. Vertical black dash lines indicate

valence band maximum (VBM) and conduction band minimum (CBM). The vertical blue dash line indicates center of band gap which mean the Fermi energy near the intrinsic level. We calculate Raman frequency using the charge state at the center of band gap. Filled stars indicate the charge transition level.

We conducted 8.33% (1 of 12 oxygens) substitutional anionic doping of representative doping element such as Carbon, Nitrogen, and Fluorine on the above mentioned particular three Oxygen site. The benefit of anionic doping strategies allow fine modification of target Raman vibrational motion of α-MoO_3 because the effect of Molybdenum ions are connected to the all oxygen atom and therefore the all vibrational modes can be affected.

Interestingly, since the Raman frequency in 472 and 995 mode is related with the thermochromic structural expansion, the reduction in these frequency by doping implies the intensification of the thermal expansion at the same temperature compared to the pristine sample and thus the intensification of the temperature-dependent color difference. We believe that this possibility of reduction in temperature for thermochromic structural evolution will be crucial strategies to intensify the visible thermochromism in metal oxides given that the metal oxides generally required larger temperature difference compared to the organic thermochromic compound.